A Simple Model of the Ice Shelf–Ocean Boundary Layer and Current

ADRIAN JENKINS

British Antarctic Survey, Natural Environment Research Council, Cambridge, United Kingdom

(Manuscript received 13 October 2015, in final form 8 March 2016)

ABSTRACT

Ocean-forced basal melting has been implicated in the widespread thinning of Antarctic ice shelves, but an understanding of what determines melt rates is hampered by limited knowledge of the buoyancy- and frictionally controlled flows along the ice shelf base that regulate heat transfer from ocean to ice. In an attempt to address this deficiency, a simple model of a buoyant boundary flow, considering only the spatial dimension perpendicular to the boundary, is presented. Results indicate that two possible flow regimes exist: a weakly stratified, geostrophic cross-slope current with upslope flow within a buoyant Ekman layer or a strongly stratified, upslope current with a weak cross-slope flow. The latter regime, which is analogous to the steady solution for a katabatic wind, is most appropriate when the ice–ocean interface is steep. For the gentle slopes typical of Antarctic ice shelves, the buoyant Ekman regime, which has similarities with the case of an unstratified density current on a slope, provides some useful insight. When combined with a background flow, a range of possible near-ice current profiles emerge as a result of arrest or enhancement of the upslope Ekman transport. A simple expression for the upslope transport can be formed that is analogous to that for the wind-forced surface Ekman layer, with curvature of the ice shelf base replacing the wind stress curl in driving exchange between the Ekman layer and the geostrophic current below.

1. Introduction

Floating ice shelves compose only 3%, by volume, of the Antarctic Ice Sheet, but they receive over 80% of the outflow of grounded ice (Rignot et al. 2013) and play a critical role in regulating that outflow. The processes of iceberg calving and basal melting that remove mass from the ice shelves are therefore of first-order importance in determining the overall mass budget of the ice sheet and hence its contribution to eustatic sea level. Basal melting in particular has been highlighted as the driver of ice shelf thinning that has been causally linked with acceleration in the outflow of grounded ice (Pritchard et al. 2012). What determines the distribution and rates of basal melting beneath an ice shelf and how these respond to changes in ocean temperature or circulation are therefore key questions.

Recent years have seen major progress in our ability to quantify basal melting beneath ice shelves (Corr et al. 2002; Jenkins et al. 2006; Rignot et al. 2013; Depoorter et al. 2013), providing a wealth of data to test the skill of numerical models of the sub–ice shelf circulation. However, the rates of mass transfer between ice and ocean that are predicted even by state-of-the-art, primitive equation models remain sensitive to the choice of poorly constrained parameters, particularly in the vertical mixing schemes used (Dansereau et al. 2014). The tight coupling between turbulent transfer to the ice and the buoyancy forcing that is a key driver of the subice circulation means that any deficiencies in the simulation of melting will have widespread impacts on the ocean dynamics that must be compensated for by adjustment of other parameters. The inevitable nonphysical tunings make simulations that are unconstrained by observation problematic.

To date we have only limited observations from within the oceanic boundary layer beneath ice shelves, and the majority of those data lack the resolution needed to understand the dynamics of, and mixing within, the boundary flows (e.g., Nicholls et al. 2009). As a result, parameterizations of the boundary layer beneath ice shelves are typically derived from the comparatively rich database of observations within the turbulent boundary layer beneath sea ice (e.g., Holland and Jenkins 1999). While the fundamental physics governing the ice–ocean boundary layer are not dependent on the form of the ice

Corresponding author address: Adrian Jenkins, British Antarctic Survey, High Cross, Madingley Road, Cambridge CB3 0ET, United Kingdom.
E-mail: ajen@bas.ac.uk

DOI: 10.1175/JPO-D-15-0194.1

cover, there are subtle differences in the forcing that alter the structure of the boundary layer.

In the case of sea ice, flow and mixing in the boundary layer are generated by wind forcing of the ice motion and the buoyancy fluxes associated with ice growth and ablation (McPhee 2008). Other than the solid upper boundary, the processes are much like those that operate elsewhere at the ocean surface. A key distinction of the ice shelf–ocean boundary layer is that the ice shelf provides a solid, static boundary overlying the ocean. Current shear within the boundary layer is produced by drag on the far-field flow driven by externally imposed pressure gradients, rather than by an externally imposed stress on the surface of an otherwise relatively slow-moving water column. The ice shelf–ocean boundary layer should thus look more like the bottom boundary layer of the ocean.

Another key difference is the large-scale slope of the boundary induced by the temporal thinning of the floating ice shelf as it flows from the grounding line to the calving front. In some respects the inverted topography of the ice base is no different from the topography of the seabed at the continental shelf edge, and the impact of a sloping boundary on processes within the bottom boundary layer has been discussed by Garrett et al. (1993), for example. However, there is a critical difference between the seabed and the ice shelf base: the latter is a reactive boundary. Hence, the stable boundary layer created by ablation of the ice shelf base is subject to a buoyancy force acting up the slope. The result should be a boundary current having a velocity maximum some distance below the ice–ocean interface and reversed shear below as the buoyancy force reduces and the current relaxes to the far-field flow. This structure is analogous to that formed by a dense current on a seabed slope that has been investigated in the context of overflows from marginal seas (Price and Baringer 1994). However, there are key differences in that the properties of an overflow are set externally by the processes supplying the dense water and subsequent mixing acts to homogenize the current and reduce the density difference. For the ice shelf–ocean boundary flow, the properties are set by its interaction with the slope and that interaction provides a continuous stabilizing buoyancy flux.

Such a boundary flow has no analog in the ocean and is most similar to the katabatic flow in the atmospheric boundary layer that is generated when there is a surface temperature inversion over sloping topography. Katabatic winds are most well-developed and persistent over the polar ice sheets where the inversion is caused by the net radiation loss at the surface (van den Broeke and van Lipzig 2003). Thus, unlike the ice shelf–ocean boundary current, the buoyancy forcing is externally imposed rather than generated by the reaction of the boundary to the physical properties of the fluid within the boundary layer. This further added complexity makes the ice shelf–ocean boundary current a fascinating fluid dynamical problem in its own right, irrespective of its importance in controlling the direct exchange of mass between ice sheets and oceans.

2. Motivation

The conceptual picture of ice shelf–ocean boundary currents has tended to be dominated by plume theory, which was first applied to the problem by MacAyeal (1985). The boundary current is assumed to be vertically well-mixed and only the depth-averaged properties are considered. This assumption draws on the analogy with density currents descending seabed slopes (Price and Baringer 1994) but may not be valid when the interaction of the boundary with the plume induces a stabilizing buoyancy flux, as is the case when an ice shelf melts. Although the three-dimensional, primitive equation models that have been applied to the problem have the potential to simulate the vertical structure of a plume, they generally lack the resolution, and arguably the physics, to simulate a buoyancy-forced boundary flow, particularly on a steep slope. Observations typically show some stratification close to the ice shelf base (Nicholls et al. 2009; Hattermann et al. 2012; Stanton et al. 2013), but measurements of the associated current profiles that result from the stratification and furthermore generate the turbulence that drives the exchange of heat, freshwater, and momentum between ice and ocean are completely lacking. Thus, there are real gaps in our understanding of the ocean flow along an ice shelf base, and filling some of those gaps is the motivation for this study.

The aim is to investigate the structure of the ice shelf–ocean boundary flow using a simple model that incorporates just one spatial dimension, perpendicular to the ice–ocean interface. Restriction to a single spatial dimension is a severe limitation in that the great success of the plume concept has been to demonstrate the fundamental role of advection within the boundary flow in setting the water properties that drive the phase changes at the ice–ocean interface. However, the aim is not to produce a complete picture of the ice shelf–ocean boundary current but rather to provide a complementary and hopefully informative insight into an aspect of sub–ice shelf flow that has received little attention to date. Furthermore, this initial study employs constant diffusivity/viscosity in order to gain fundamental insight into the nature of what is effectively a stratified Ekman layer on a slope. Inclusion of a more realistic turbulence closure would be a simple extension of the model that is left for a later study. The limitations of the model leave a number of questions about real world ice shelf boundary flows unanswered, but what does emerge is an alternative

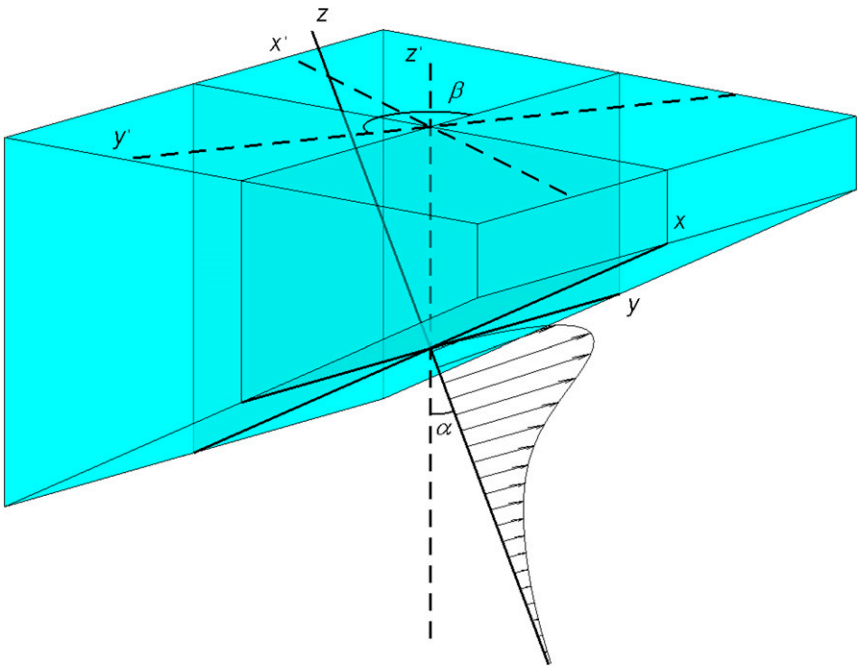

FIG. 1. Schematic diagram illustrating the assumed ice geometry and the transformed coordinate system in which the model is formulated. Conventional (dashed) coordinate axes are zonal, positive eastward (x'); meridional, positive northward (y'); and vertical, positive upward, zero at sea level (z'). The transformed (solid) system (x, y, z) has its origin at the ice–ocean interface and axes that point upslope, across slope, and perpendicular to the ice–ocean interface, respectively. The two rotations needed to transform the axes are denoted by angles β and α. Arrows show velocity vectors for a typical current profile (Fig. 2f).

conceptual picture of the boundary layer and current that may help to shape future observation and modeling of ice shelf–ocean interactions.

3. Model

The starting points for the derivation of the model are the conservation equations for mass and momentum written for conventional x' (zonal), y' (meridional), and z' (vertical) coordinates:

$$\frac{D\rho}{Dt} + \rho\nabla\cdot\mathbf{U} = 0,$$

$$\rho\frac{D\mathbf{U}}{Dt} + \rho 2\boldsymbol{\Omega}\times\mathbf{U} = -\nabla P - \rho g\mathbf{k} + \nabla\cdot(\rho\nu\nabla\cdot\mathbf{U}).$$

In the above equations, $\mathbf{U}$ is a three-dimensional current vector, P is pressure, t is time, ρ is water density, ν is eddy viscosity, $\boldsymbol{\Omega}$ is Earth's rotation vector, g is the acceleration due to gravity, and $\mathbf{k}$ is a unit vector in the local vertical direction (z'). The ice–ocean interface is assumed to be a planar surface that makes an angle α with the horizontal. A transformed coordinate system is defined by translation along z' to set the origin at the ice–ocean interface; rotation about z' to give a y axis aligned with the ice–ocean interface, perpendicular to the slope vector; then rotation about y to give an x axis following the ice–ocean interface, pointing directly upslope, and a z axis normal to the interface (Fig. 1). Applying the above transformations and the Boussinesq approximation gives

$$\nabla\cdot\mathbf{U} = 0,$$

$$\frac{Du}{Dt} + 2\Omega[(\cos\theta\cos\beta)w - (\cos\theta\sin\beta\sin\alpha + \sin\theta\cos\alpha)v] = -\frac{1}{\rho_0}\frac{\partial P}{\partial x} - \frac{\rho}{\rho_0}g\sin\alpha + \nabla\cdot(\nu\nabla u),$$

$$\frac{Dv}{Dt} + 2\Omega[(\cos\theta\sin\beta\sin\alpha + \sin\theta\cos\alpha)u + (\cos\theta\sin\beta\cos\alpha - \sin\theta\sin\alpha)w] = -\frac{1}{\rho_0}\frac{\partial P}{\partial y} + \nabla\cdot(\nu\nabla v), \quad \text{and}$$

$$\frac{Dw}{Dt} + 2\Omega[(\cos\theta\sin\beta\cos\alpha + \sin\theta\sin\alpha)v - (\cos\theta\cos\beta)u] = -\frac{1}{\rho_0}\frac{\partial P}{\partial z} - \frac{\rho}{\rho_0}g\cos\alpha + \nabla\cdot(\nu\nabla w),$$

where (u, v, and w) are components of the current vector in the transformed (x, y, and z) system, Ω is the magnitude of Earth's rotation vector, θ is latitude, β is the true bearing of the y axis (Fig. 1), and ρ_0 is a reference density.

The hydrostatic approximation is applied in the direction perpendicular to the ice shelf base (z), so that the last equation reduces to

$$0 = \frac{\partial P}{\partial z} + \rho g \cos\alpha .$$

The pressure as a function of distance from the interface is then given by

$$P(-z) = P(\eta) + g\cos\alpha \int_{-z}^{\eta} \rho \, dz ,$$

where η is the instantaneous deviation of the ice–ocean interface from its equilibrium position ($z = 0$), and this leads to the following expression for the pressure gradient parallel to the ice–ocean interface:

$$\nabla P(-z) = \nabla P(\eta) + g\cos\alpha \left[\rho(\eta)\nabla\eta + \int_{-z}^{\eta} \nabla\rho \, dz \right].$$

The ice thickness is assumed constant in time, so the pressure it exerts at the ocean surface $P(\eta)$ can be defined in terms of a reference state where the planar ice surface is floating in stationary, ambient fluid of density ρ_a. This then defines the reference position about which deviations η generate an additional pressure gradient force. The pressure gradient imposed by the ice shelf is

$$\frac{\partial P(\eta)}{\partial x} = -\rho_a g \sin\alpha, \quad \text{and}$$
$$\frac{\partial P(\eta)}{\partial y} = 0 ,$$

and the full pressure gradient parallel to the ice–ocean interface can be written as

$$\frac{\partial P}{\partial x} = -\rho_a g \sin\alpha + \rho_0 g \cos\alpha \frac{\partial \eta}{\partial x} - \rho_0 g \cos\alpha \int_{-z}^{\eta} \frac{\partial \Delta\rho}{\partial x} dz, \quad \text{and}$$
$$\frac{\partial P}{\partial y} = \rho_0 g \cos\alpha \frac{\partial \eta}{\partial y} - \rho_0 g \cos\alpha \int_{-z}^{\eta} \frac{\partial \Delta\rho}{\partial y} dz ,$$

where

$$\Delta\rho = \frac{\rho_a - \rho}{\rho_0}$$

has been introduced to remove the stationary reference state and, consistent with the Boussinesq approximation, the reference density has been used in place of $\rho(\eta)$. Note that the ambient density is retained in the term that specifies the pressure gradient associated with the slope of the ice shelf base. The slope generated by the static ice thickness gradient can be many orders of magnitude larger than the transient slopes related to ocean dynamics, so a small error in the density multiplying the static slope would lead to a large error in the pressure gradient.

The density is a function of temperature T and salinity S, for which conservation equations (with constant factors of reference density and specific heat capacity removed) are

$$\frac{DT}{Dt} = \nabla \cdot (K_T \nabla T), \quad \text{and}$$
$$\frac{DS}{Dt} = \nabla \cdot (K_S \nabla S),$$

where K_T and K_S are eddy diffusivities for heat and salt, respectively. The above equations form a fairly complete model of the ice shelf–ocean boundary layer, from which a number of reduced models can be derived. For example, depth integration would yield a plume model in terrain-following coordinates; then dropping time dependence, cross-slope gradients, the Coriolis acceleration, and the pressure gradient associated with along-stream variations in plume properties would yield the basic one-dimensional plume model of Jenkins (1991). To construct a reduced model suitable for investigating the structure of the boundary layer normal to the ice–ocean interface, all gradients in ocean properties parallel to the interface are assumed to be zero, and only derivatives with respect to time and the normal coordinate are retained. With these assumptions, the continuity equation becomes

$$\frac{\partial w}{\partial z} = 0 ,$$

which implies that the velocity normal to the boundary is constant and therefore must be equal to the melt rate everywhere. Since the melt rate is so much (typically six orders of magnitude) smaller than the other velocities, the vertical velocity is assumed to be zero, and melting is treated as a sink of heat and salt. This has the further advantage of reducing the problem to one of pure diffusion. The appropriate equations are

$$\frac{\partial u}{\partial t} - \phi v = \Delta\rho g \sin\alpha - g\cos\alpha \frac{\partial \eta}{\partial x} + \frac{\partial}{\partial z}\left(\nu \frac{\partial u}{\partial z}\right),$$
$$\frac{\partial v}{\partial t} + \phi u = -g\cos\alpha \frac{\partial \eta}{\partial y} + \frac{\partial}{\partial z}\left(\nu \frac{\partial v}{\partial z}\right),$$
$$\frac{\partial T}{\partial t} = \frac{\partial}{\partial z}\left(K_T \frac{\partial T}{\partial z}\right), \quad \text{and}$$
$$\frac{\partial S}{\partial t} = \frac{\partial}{\partial z}\left(K_S \frac{\partial S}{\partial z}\right),$$

where the Coriolis parameter is given by

$$\phi = 2\Omega(\cos\theta \sin\beta \sin\alpha + \sin\theta \cos\alpha).$$

Note that all components of Earth's rotation vector have been retained, so the equations remain valid for all slope angles from horizontal to vertical ($0 \le \sin\alpha \le 1$).

The equations are closed with the addition of a linear equation of state:

$$\Delta\rho = \beta_S(S_a - S) - \beta_T(T_a - T),$$

where T_a and S_a are the ambient temperature and salinity, respectively. The two momentum equations can be conveniently combined by adopting complex notation for the vectors:

$$\frac{\partial \mathbf{u}}{\partial t} + \phi i\mathbf{u} = \Delta\rho g \sin\alpha - g\cos\alpha\nabla\eta + \frac{\partial}{\partial z}\left(\nu\frac{\partial \mathbf{u}}{\partial z}\right), \quad (1)$$

where

$$\mathbf{u} = u + iv, \quad \nabla\eta = \frac{\partial\eta}{\partial x} + i\frac{\partial\eta}{\partial y}.$$

Contraction of the scalar equations is also possible through the introduction of the thermal driving T_* as a new dependent variable:

$$T_* = T - [\lambda_1 S + \lambda_2 + \lambda_3 P(\eta)],$$

where λ_1, λ_2, and λ_3 are coefficients in a linearized expression for the freezing point of seawater as a function of salinity and pressure (Jenkins 2011). A linear combination of the two scalar equations then yields a single equation in the thermal driving

$$\frac{\partial T_*}{\partial t} = \frac{\partial}{\partial z}\left(K\frac{\partial T_*}{\partial z}\right), \quad (2)$$

where it has been assumed that the diffusivity $K = K_T = K_S$, which is reasonable throughout most of the turbulent boundary layer.

For use with (1) and (2), the equation of state can be conveniently rewritten in terms of T_*:

$$\Delta\rho = (T_{*a} - T_*)\left[\frac{\beta_S - \beta_T(T_a - T)/(S_a - S)}{(T_a - T)/(S_a - S) - \lambda_1}\right]. \quad (3)$$

Note that up to this point the only stipulation on the ambient conditions is that they represent a motionless state, and they could therefore include a horizontally uniform vertical stratification. However, in most of what follows the ambient temperature and salinity are taken to be constant. With this restriction, cooling and dilution within the boundary layer are related by a constant factor (Gade 1979) that depends only on the ambient conditions and the specified core temperature of the ice shelf relative to the freezing point at the interface T_{*i}:

$$\frac{(T_a - T)}{(S_a - S)} = \frac{T_{*a} + (L_i - c_i T_{*i})/c}{S_a}, \quad (4)$$

where c is specific heat capacity, L is latent heat of fusion, and the "i" subscript indicates ice properties. Since the temperature difference between the ice shelf core and the ice–ocean interface is at least an order of magnitude more than variations in the interface temperature driven by salinity changes there, T_{*i} is assumed to be constant. With this assumption the relationship between $\Delta\rho$ and T_* is linear.

Boundary conditions for (1) and (2) are

$$\mathbf{u} = 0, \quad T_* = 0 \quad \text{at} \quad z = 0;$$

$$\mathbf{u} = \frac{ig\nabla\eta}{\phi}, \quad T_* = T_{*a} \quad \text{at} \quad z = \infty;$$

and the far-field properties also provide the initial conditions over the entire water column. The velocity boundary conditions complete the specification of a standard model of the Ekman layer created either by a far-field geostrophic flow (Garrett et al. 1993) or by a density current (Wang et al. 2003) over a sloping solid boundary, while the thermal driving boundary conditions encapsulate the distinctive nature of this problem. The zero-flux Neumann boundary condition that would conventionally be applied at the seabed is replaced with a Dirichlet boundary condition that enforces the freezing point condition. Thus, when the far-field thermal driving is nonzero, turbulent diffusion of heat through the boundary layer causes it to stratify. The situation is thus fundamentally different from those studied by Garrett et al. (1993), in that they considered boundary mixing as a process of destroying the stratification imposed by the far-field conditions, and Wang et al. (2003), in that they defined the density deficit over the slope as a constant forcing parameter.

The only remaining problem is to specify ν and K, which in general would be specified as functions of depth via a turbulence closure scheme of arbitrary complexity. As mentioned above, the present study uses the simplest possible closure, that of equal, constant values. This is attractive in that it is straightforward to implement and easy to understand yet allows some key features of the boundary layer structure to emerge.

A problem that is immediately apparent from the above model setup is that there is no steady-state solution. The system will continue to evolve until the heat flux is

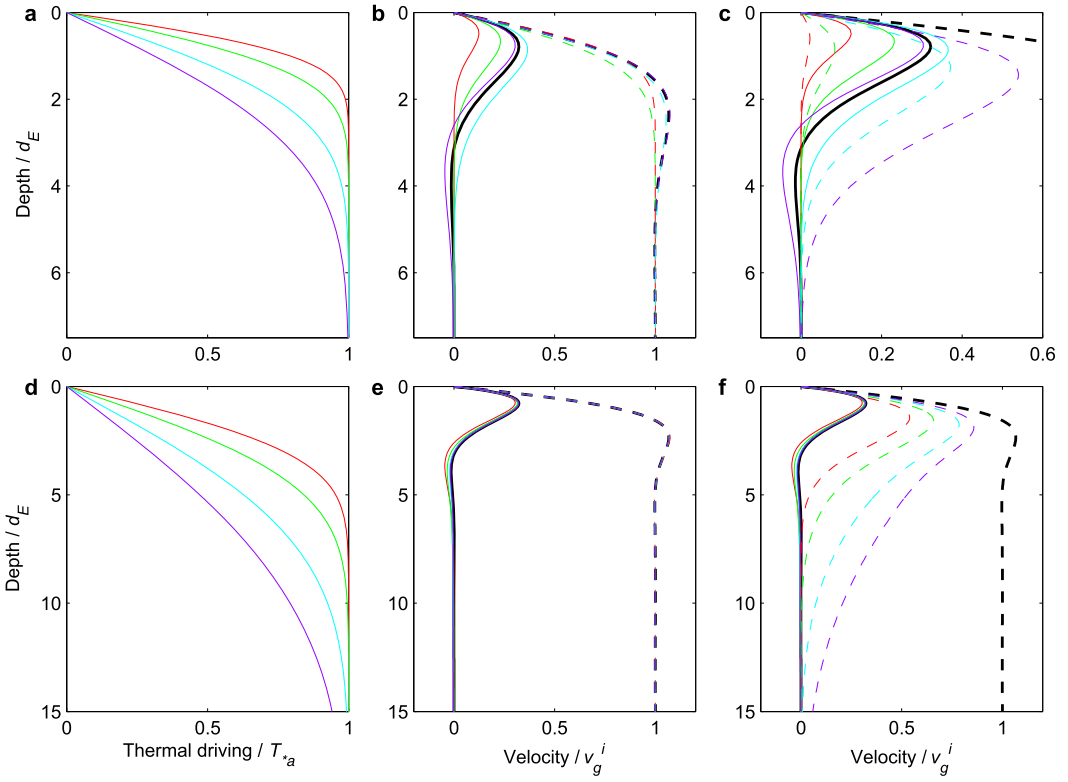

FIG. 2. (a),(d) Thermal driving and upslope (solid) and across-slope (dashed) velocity components as a function of distance from the ice–ocean interface for a flow forced by (b),(e) a background pressure gradient and (c),(f) an inclined ice surface. Different colors indicate the solution (top) after 0.1 (red), 0.2 (green), 0.5 (cyan), and 1 (magenta) inertial period and (bottom) after 1 (red), 2 (green), 5 (cyan), and 10 (magenta) inertial periods. Thick black lines show the analytical solution for the steady Ekman layer formed by a uniform background flow. The depth and velocity scales d_E and v_g^i are the Ekman depth, given by (6), and the geostrophic velocity at the interface, given by $(g/\phi)\partial\eta/\partial x$ for the pressure gradient forcing in (b) and (e) and (7) for the sloping ice shelf base in (c) and (f). Note the differing vertical and horizontal scales.

everywhere equal. There are two ways around this problem, both of which require a relaxation of the zero gradient assumption parallel to the ice–ocean interface. The first is to impose an "entrainment" velocity perpendicular to the interface that drives divergence in the boundary current. The velocity perpendicular to the interface is then given by

$$w = \frac{z}{z_{\rm bc}} w_e \quad \text{for} \quad 0 \geq -z \geq -z_{\rm bc}, \quad \text{and}$$
$$w = w_e \quad \text{for} \quad -z \leq -z_{\rm bc}, \tag{5}$$

where the thickness of the boundary current $z_{\rm bc}$ is defined by the level at which the deviation from the imposed far-field flow rises above a threshold value. Vertical advection can then support a divergence in the heat flux perpendicular to the interface. The small divergence in the flow parallel to the interface is ignored in the momentum balance to avoid the need for a more complex model. The alternative way to generate a steady state is to impose a thermal driving gradient parallel to the interface, so that advection by the boundary flow can support a divergence in the heat flux toward the interface. The choices of either entrainment velocity or boundary-parallel temperature gradient are arbitrary, as are the steady states they produce, but the alternative is to choose an arbitrary instant from a continuously evolving solution. None of these choices are entirely satisfactory, and this is one of the limitations alluded to earlier.

4. Results

a. *Current structures generated by pressure gradient and buoyancy forcing*

Figure 2 shows profiles of thermal driving and boundary-parallel velocity components for two simple configurations of the model: one driven by a depth-independent pressure gradient set up by deviations in the height of an otherwise horizontal ice–ocean interface, the other

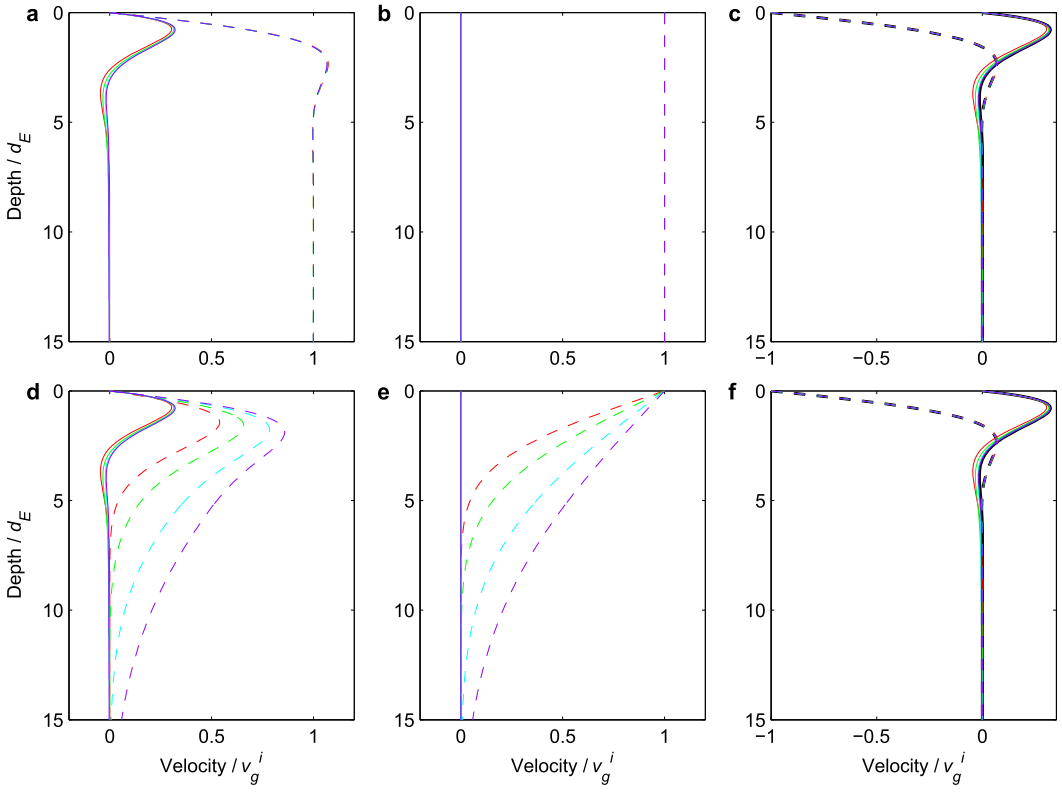

FIG. 3. (a),(d) Current profiles from Figs. 2e and 2f at (a),(d) 1, 2, 5, and 10 inertial periods and their decomposition into (b),(e) geostrophic and (c),(f) ageostrophic components. Thick black lines in (c) and (f) show the analytical solution for the steady Ekman layer.

driven by a depth-dependent pressure gradient set up by the density deficit generated at a sloping ice–ocean interface. In both cases the zero thermal driving condition at the ice–ocean interface creates a step that diffuses into the ambient water column. Since the eddy diffusivity is constant, the solution is unaffected by the differing current structure and evolves independently, producing a broadening thermal boundary layer with gradually weakening stratification (Figs. 2a,d).

For a horizontal ice–ocean interface with subice flow forced by a surface pressure gradient, the dynamic solution is unaffected by the stratification and conforms to that of the classic Ekman layer (Figs. 2b,e). The far-field geostrophic flow is reduced to zero over the depth of the Ekman layer, within which there is a frictionally generated current that flows to the right (in the Southern Hemisphere) of the geostrophic current. Over the first inertial period both thermal and velocity boundary layers are of the same depth (Fig. 2a), but subsequently the thermal boundary layer continues to grow (Fig. 2d), while the velocity profile reaches a steady state, with deviations from geostrophy confined to the Ekman layer (Fig. 2e).

The continued growth of the thermal boundary layer becomes important when a slope is introduced to the ice–ocean interface, providing a link between the thermal and current structures. The buoyancy forcing produces currents wherever there is a thermal driving deficit (Figs. 2c,f). As before, currents beyond the Ekman layer are purely geostrophic, flowing at right angles to the forcing created by the ice shelf basal slope, but in this case they decay to zero in line with the buoyancy forcing. For times longer than the inertial period the frictionally generated deviations from the evolving geostrophic flow are steady and follow the classic Ekman layer solution (Fig. 3).

To obtain that solution, (1) and (2) can be recast in terms of a time-dependent, cross-slope, geostrophic current $(0, v_g,)$ and a steady deviation from that current (u', v'):

$$-\phi(v_g + v') = \Delta\rho g \sin\alpha + K\frac{\partial^2 u'}{\partial z^2},$$

$$\frac{\partial v_g}{\partial t} + \phi u' = K\frac{\partial^2}{\partial z^2}(v_g + v'), \quad \text{and}$$

$$\frac{\partial \Delta\rho}{\partial t} = K\frac{\partial^2 \Delta\rho}{\partial z^2}.$$

The geostrophic current is given by

$$-\phi v_g = \Delta\rho g \sin\alpha,$$

so the scalar equation implies an analogous evolution equation for the geostrophic velocity

$$\frac{\partial v_g}{\partial t} = K\frac{\partial^2 v_g}{\partial z^2}.$$

Making use of this in the momentum equations, the expression for the deviations from geostrophy become the conventional ones for the Ekman layer,

$$-\phi v' = K\frac{\partial^2 u'}{\partial z^2}, \quad \text{and}$$
$$\phi u' = K\frac{\partial^2 v'}{\partial z^2},$$

for which the solution is well known (Cushman-Roisin and Beckers 2011):

$$u' = v_g^i \exp\left(\frac{-z}{d_E}\right)\sin\left(\frac{z}{d_E}\right), \quad \text{and}$$
$$v' = v_g^i \exp\left(\frac{-z}{d_E}\right)\cos\left(\frac{z}{d_E}\right),$$

where d_E is the Ekman depth

$$d_E = \sqrt{\frac{2K}{|\phi|}}, \tag{6}$$

and v_g^i is the geostrophic velocity that would be attained at the ice–ocean interface in the absence of friction. The above analytical solutions for the steady Ekman currents are shown in Fig. 3f. They are identical to the classical Ekman currents (Fig. 3c) but are scaled by the hypothetical maximum geostrophic current, associated with the maximum in buoyancy forcing at the ice–ocean interface, rather than the far-field geostrophic flow, which in this case is zero. The maximum geostrophic current can be conveniently written in terms of the far-field thermal driving and ice shelf basal slope:

$$v_g^i = \frac{g}{\phi}\sin\alpha\frac{\Delta\rho}{\Delta T_*}(T_{*_a} - T_*^i), \tag{7}$$

where T_*^i is the thermal driving at the ice–ocean interface [$T_*^i = 0$ is imposed by the Dirichlet boundary condition for an ice–ocean interface, but the term is retained in (7) for generality], and the factor that relates the density deficit to thermal driving can be derived from (3) and (4) as

$$\frac{\Delta\rho}{\Delta T_*} = \frac{S_a\beta_S - \beta_T[T_{*_a} + (L_i - c_i T_{*_i})/c]}{T_{*_a} + (L_i - c_i T_{*_i})/c - S_a\lambda_1}. \tag{8}$$

For typical ice and ocean conditions, (8) has an approximately constant value of around 2.5×10^{-4}. For quasi-horizontal flows, where $|\phi|$ is around 1.4×10^{-4}, the maximum geostrophic velocity is therefore given approximately by

$$v_g^i \approx 17.5 \sin\alpha T_{*_a}.$$

The decomposition of the boundary-parallel currents (Fig. 3) effectively recasts the upslope flow as the Ekman transport associated with a cross-slope, buoyancy-driven, geostrophic current and motivates the introduction of some useful terminology that will be adopted throughout this paper to clarify the ensuing discussion. The layer of the ocean that has been influenced by the ice shelf and is hence partially or wholly forced by the associated buoyancy will be referred to as a buoyant "boundary current." Within that current, the part that is influenced by boundary friction will be referred to as the "boundary layer." Thus, the boundary layer has an upslope, frictionally driven velocity component, while the boundary current beyond the boundary layer is purely geostrophic.

For small slopes, when the conventional approximation for the Coriolis parameter ($\phi \approx 2\Omega\sin\theta\cos\alpha$) is valid, the geostrophic velocity in (7) is the same as that derived by Nof (1983) for the speed of a density anomaly across a frictionless slope. Furthermore, the current structures in Figs. 2 and 3 are analogous to those found for the downslope flow of dense water (Shapiro and Hill 1997; Wang et al. 2003; Cenedese et al. 2004). However, there are some important differences, illustrated in Fig. 4, which shows the results obtained when (1) and (2) are applied to the gravity current problem by switching the Dirichlet boundary condition on (2) to a zero-flux Neumann condition after the first inertial period. Mixing now homogenizes the boundary current, reducing the density deficit at the interface (Fig. 4a). For the case of a background pressure gradient and no interfacial slope the change in stratification has no impact (Fig. 4b), but for a sloping interface the decrease in the buoyancy forcing reduces the magnitude of the currents (Fig. 4c). Note that as in Fig. 3, (7), with T_*^i now freely evolving, accurately scales the frictional response (Figs. 4d,f) irrespective of the density profile through the boundary layer. For the ice shelf–ocean boundary current, where the thermal driving at the interface is fixed at zero, the frictional response of the boundary layer is thus fixed in time, despite the continuous evolution of

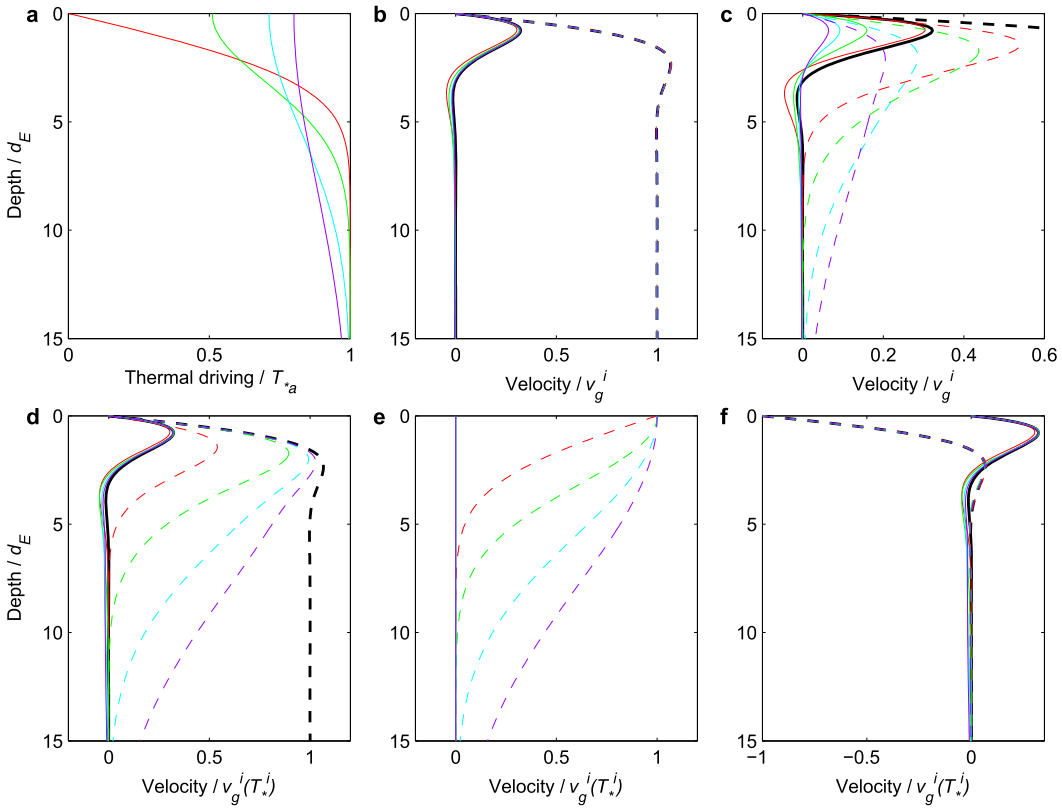

FIG. 4. (a) Thermal driving and upslope (solid) and across-slope (dashed) velocity components as a function of distance from the ice–ocean interface for a conventional density current forced by (b) a background pressure gradient and (c) an inclined surface. Different colors indicate the solution after 1, 2, 5, and 10 inertial periods, and bold black lines show the Ekman solution (as in Fig. 2). Forcing is identical to that used in Fig. 2, but with the upper Dirichelet boundary condition on thermal driving replaced by a zero-flux Neumann condition after one inertial period. Lower panels show the velocity profiles in (c) replotted (d) with time-varying scaling calculated using the instantaneous value of the interfacial thermal driving, T_*^i, in (a) and the decomposition into (e) geostrophic and (f) ageostrophic components. Note the differing horizontal scale in (c).

the stratification and flow across the entire boundary current. Herein lies the principal difference between the flow along a reactive boundary discussed in this paper and the flow of dense current down a passive seabed slope.

b. *Combinations of pressure gradient and buoyancy forcing*

When there is a background pressure gradient forcing the flow on a sloping ice shelf base, the solutions for both the geostrophic (Figs. 3b,e) and ageostrophic (Figs. 3c,f) parts of the flow generated by each component of the forcing are additive. A pressure gradient applied along-slope generates geostrophic across-slope and frictional along-slope currents that work with or against the buoyancy-forced analogs. Thus, a geostrophic current flowing with deepening ice to its left (in the Southern Hemisphere) enhances both across-slope flow and the upslope Ekman transport in the boundary layer (Figs. 5a–c), while a current in the opposite direction opposes both (Figs. 5d–f). In the case that the pressure gradient–forced geostrophic flow is exactly equal and opposite to v_g^i, the boundary layer is arrested (Fig. 5e); there is no ageostrophic flow at all, and the geostrophic flow is brought to zero at the interface by the opposing buoyancy and pressure gradient forcing. For a pressure gradient–forced geostrophic current that exceeds $-v_g^i$, the forcing on the boundary layer exceeds that associated with the opposing buoyancy-forced current and the transport in the boundary layer is downslope (Fig. 5f). With high slopes and thermal driving, the buoyancy forcing from ice shelf melting dominates over any reasonable background flows, so current profiles will look like those in Figs. 5a and 5d, but at low slopes and thermal driving conditions common beneath Antarctic ice shelves, arrest and reversal of the upslope flow can occur and all of Figs. 5a–f are possible.

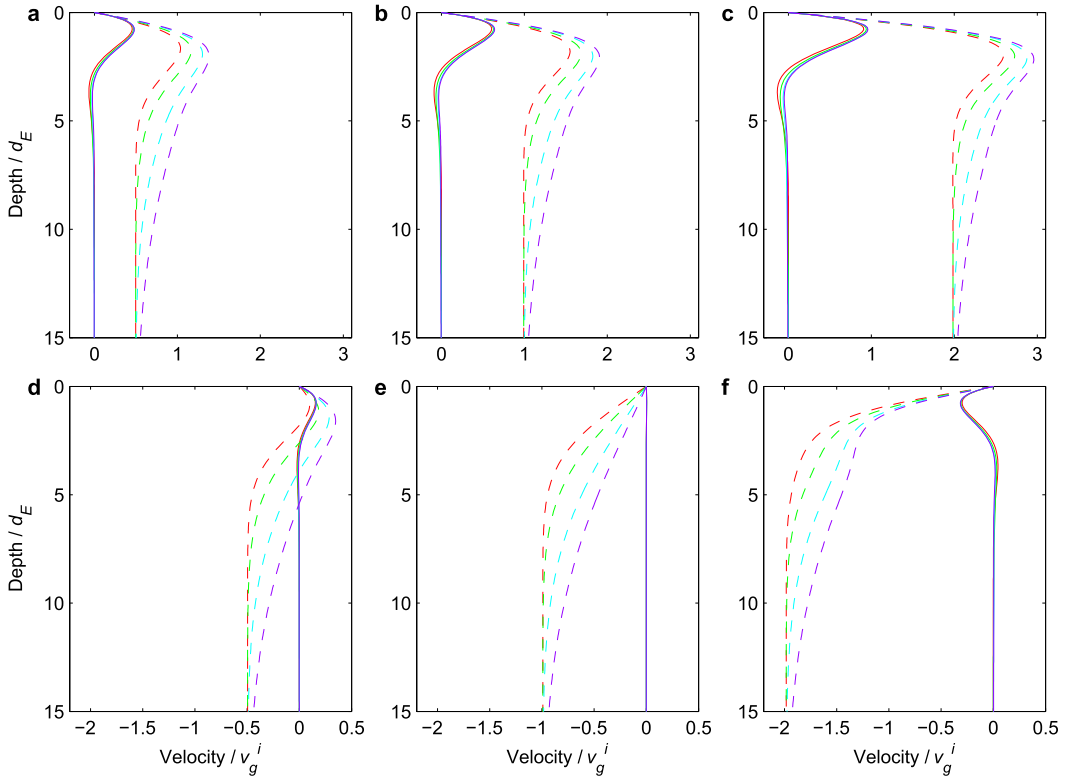

FIG. 5. Upslope (solid) and across-slope (dashed) velocity profiles generated by a combination of an inclined ice surface and an along-slope background pressure gradient. The magnitude of the along-slope pressure gradient is chosen to give a cross-slope geostrophic flow equal to (a) $v_g^i/2$, (b) v_g^i, (c) $2v_g^i$, (d) $-v_g^i/2/2$, (e) $-v_g^i$, and (f) $-2v_g^i$, where v_g^i is given by (7). Different colors indicate the solution after 1, 2, 5, and 10 inertial periods.

Beneath an ice shelf, the water column thickness gradients that determine the background potential vorticity (ϕ/H) gradients result from the combination of seabed and ice base topography. Thus, unlike in the open ocean, it is possible to have geostrophic currents that flow up or down the ice shelf base in response to cross-slope pressure gradients. For a geostrophic flow in the downslope direction, the associated Ekman transport is in the same sense as the cross-slope buoyancy-forced flow, so that the cross-slope flow is enhanced within the boundary layer (Figs. 6a–c). If the downslope geostrophic current is weaker than the upslope Ekman current, there is a reversal in the along-slope flow within the boundary layer with upslope flow along the ice shelf base giving way to downslope flow further from the interface (Fig. 6a). Otherwise there is downslope flow at all depths (Figs. 6b,c). For an upslope geostrophic flow, the associated Ekman transport opposes the cross-slope, buoyancy-forced current (Figs. 6d–f) and if strong enough can drive a reversal in the cross-slope flow within the boundary layer (Fig. 6f). Once again, strong buoyancy forcing, caused by steep slopes and/or high thermal driving, favors the current profiles depicted in Figs. 6a and 6d, but the other forms are possible where slopes are low and thermal driving small.

Despite the simplicity of the model presented thus far, the solutions that emerge contain a rich variety of current structures. Nevertheless, the principle remains that the structure is made up from the addition of the background geostrophic flow with its associated boundary layer and the buoyancy-driven, geostrophic boundary current with its associated boundary layer. In both cases the frictionally controlled currents in the boundary layer follow the classic Ekman layer solution scaled with the free geostrophic current at the ice–ocean interface (equal to the far-field geostrophic current in the case of the depth-independent, pressure gradient–forced flow). The Ekman response that distinguishes the boundary layer from the remainder of the boundary current is steady in time, after the initial inertial oscillation, given steady forcing. However, the entire boundary current continues to evolve and would do so until the thermal driving profile were linear between the bottom boundary condition and the interface. This evolution leads to a broadening of the boundary current and a weakening of the stratification across it.

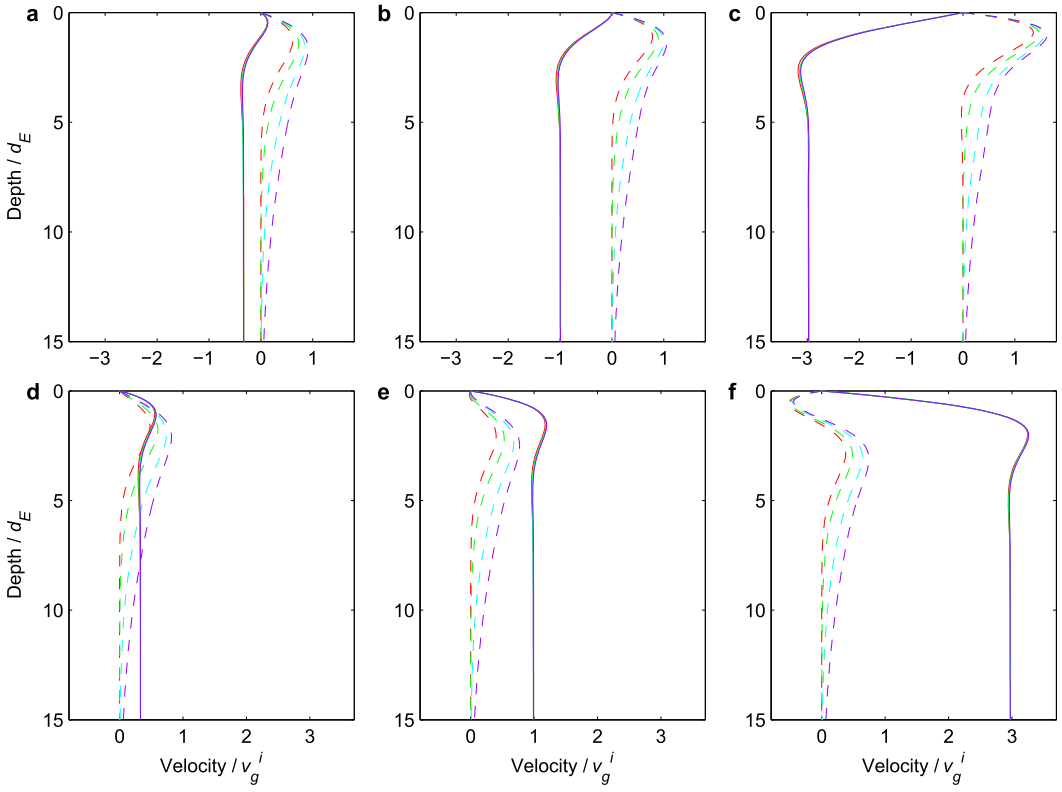

FIG. 6. Upslope (solid) and across-slope (dashed) velocity profiles generated by a combination of an inclined ice surface and an across-slope background pressure gradient. The magnitude of the across-slope pressure gradient is chosen to give an upslope geostrophic flow equal to (a) $-v_g^i/3$, (b) $-v_g^i$, (c) $-3v_g^i$, (d) $v_g^i/3$, (e) v_g^i, and (f) $3v_g^i$, where v_g^i is given by (7). Different colors indicate the solution after 1, 2, 5, and 10 inertial periods.

While the discussion thus far has focused on steady forcing, for many ice shelves the strongest pressure gradient forcing arises from perturbations in surface elevation associated with the tides. Figure 7 shows the impact of a sinusoidally varying pressure gradient applied along- and across-slope separately at frequencies equal to 2, 1, and 0.5 times the inertial frequency. For a typical polar location the first would correspond to a higher harmonic, the second a semidiurnal, and the third a diurnal tide. The amplitude of the forcing is chosen to give tidal currents having a similar order of magnitude to the buoyancy-driven flow. The response is complex, but in general the semidiurnal tide gives rise to a forced inertial oscillation, which is the same, apart from the phase, irrespective of the direction of the forcing (Figs. 7b,e), while for the diurnal tide the response is strongest in the velocity component perpendicular to the forcing, particularly within the boundary layer (Figs. 7c,f), and for the higher harmonic it is strongest parallel to the forcing (Figs. 7a,b). Arguably the most striking feature of Fig. 7 is that although the free-stream tidal currents are of comparable magnitude, there are marked differences in the current shear generated in the upper part of the water column. For the semidiurnal tide there are relatively large changes in shear across the boundary current but comparatively small changes across the boundary layer itself, particularly near the interface (Figs. 8b,e). The opposite is true for the higher- and lower-frequency forcing; the current structure of the boundary current is relatively unaffected, particularly for the higher harmonic (Figs. 8a,d), but there are marked changes in the current structure across the boundary layer that yield particularly large changes in shear stress at the ice–ocean interface when the along-slope pressure gradient varies at diurnal frequencies (Fig. 8c).

c. *Steady-state solutions including advection*

The solutions discussed above are all transient as a result of the continuous diffusive expansion of the boundary current. There are two processes that can bring a halt to that expansion: advection of heat parallel to the interface driven by along-flow gradients in thermal driving within the boundary current, and advection of heat perpendicular to the interface driven by along-flow gradients in the velocity of the boundary current.

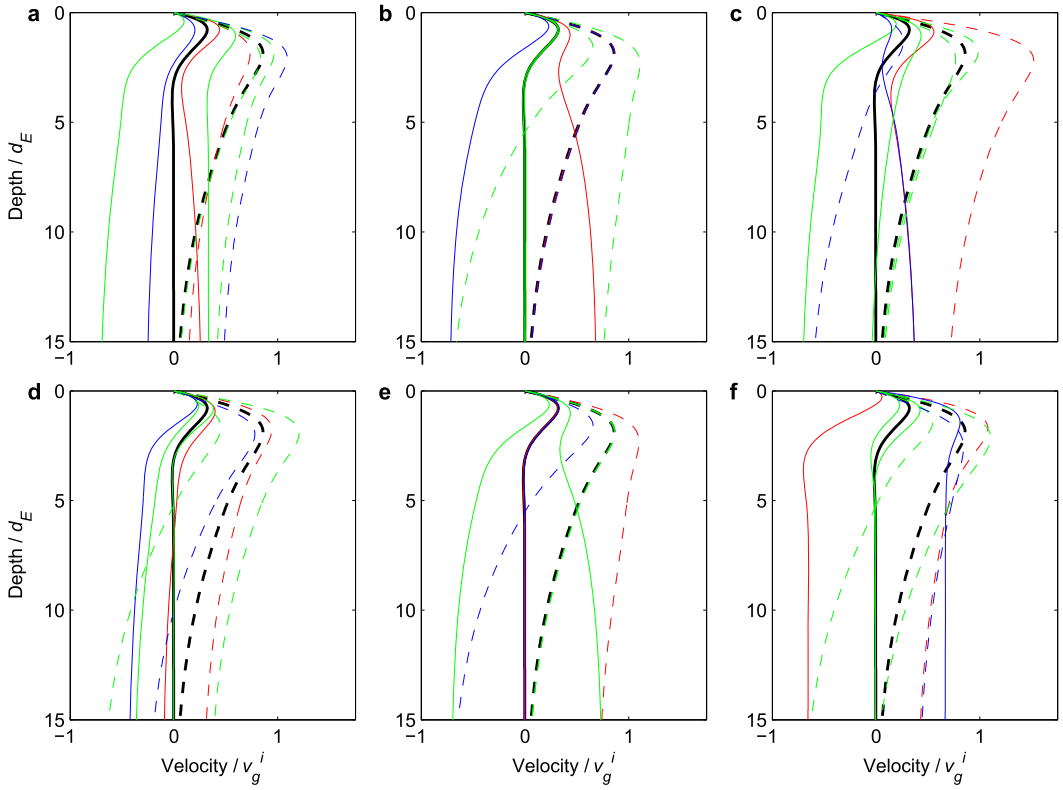

FIG. 7. Upslope (solid) and across-slope (dashed) velocity profiles generated by a combination of an inclined ice surface and a sinusoidally varying background pressure gradient applied (top) along slope, for which steady forcing yields the solutions in Fig. 5, and (bottom) across slope, for which steady forcing yields the solutions in Fig. 6. The frequency of the forcing is equal to (a),(d) twice the inertial frequency, (b),(e) the inertial frequency, and (c),(f) half the inertial frequency. Different colors indicate different states of the tide ranging from red at times of maximum pressure gradient forcing in the positive direction to green at times of zero forcing to blue at times of maximum forcing in the negative direction. Results are taken from the first tidal cycle following a spinup of 10 inertial periods. Thick black lines show the solution after 10 inertial periods with no pressure gradient forcing (as in Fig. 2f).

Figures 9a and 9d show an example solution with the addition of a velocity normal to the ice–ocean interface, as in (5). The boundary current reaches a steady thickness when advection of heat toward the boundary is sufficient to balance the diffusive loss of heat to the ice. A similar steady solution is obtained through the addition of a cross-slope gradient in thermal driving (Figs. 9b,e). The imposed gradient is such that advection by the geostrophic flow causes warming of the water column, and a steady state is reached when the boundary current carries enough heat to balance vertical diffusion toward the ice. In either case the basic structure differs little from the transient solutions discussed earlier, and the point at which the evolution has been halted is arbitrary.

An alternative to the latter solution is to add an alongslope gradient in thermal driving. However, to produce a steady solution then requires that sufficient heat be advected within the boundary layer itself to balance the heat loss to the ice. The solution (Figs. 9c,f) looks quite distinct, with strong stratification across a thin boundary layer that has a dominant upslope velocity component. The weak, cross-slope flow is frictionally driven, with the maximum occurring on the far side of the upslope velocity maximum. This solution is closest to the Prandtl model for the katabatic wind (Oerlemans 2010), which is derived from a balance between vertical diffusion and downslope advection. While the current structure is similar to those derived by Wang et al. (2003) and Cenedese et al. (2004) for dense slope flows that are thin relative to the Ekman depth, in those studies the thickness and uniform properties of the bottom layer were prescribed. The solution shown in Figs. 9c and 9f is distinct in that the thickness of, and strong stratification across, the upslope flow are derived parameters.

It is instructive to look more closely at the solution for this regime, which can be described by a set of equations that are analogous to those from which the earlier

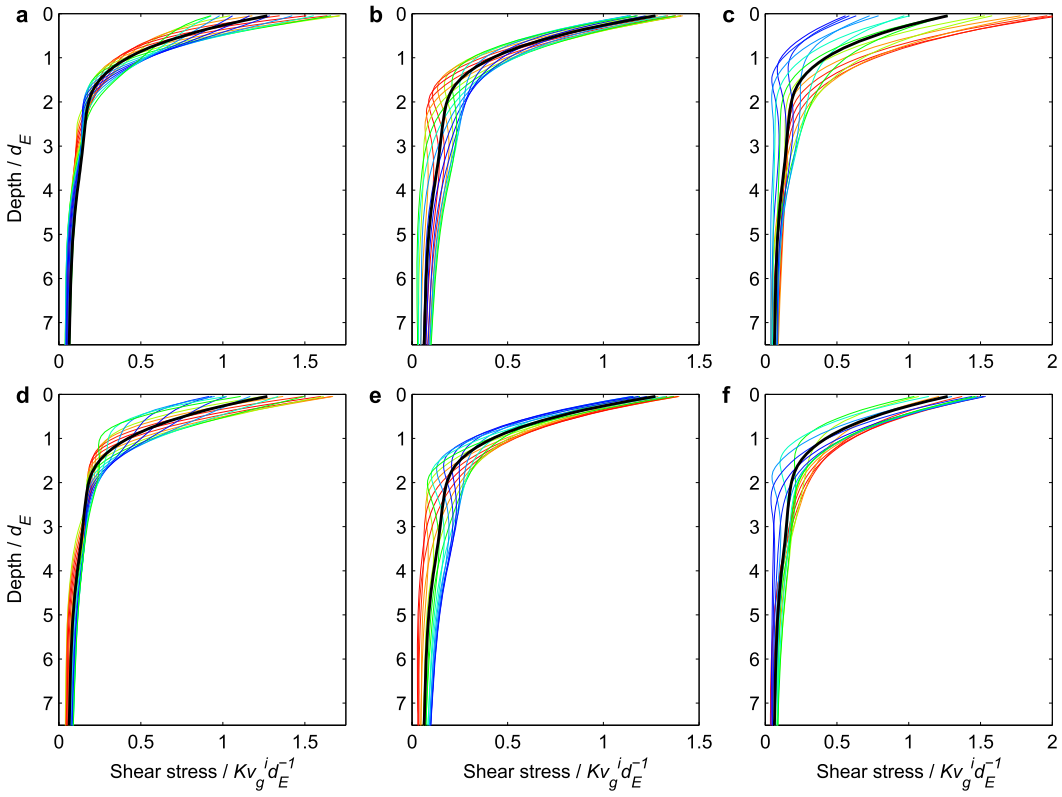

FIG. 8. Shear stress profiles for the corresponding tidally varying velocity profiles shown in Fig. 7. Different colors indicate different states of the tide. In addition to the red, green, and blue profiles corresponding to the velocity profiles in Fig. 7, three intermediate profiles are included through each quarter cycle of the forcing. Thick black lines show the shear stress associated with the bold black velocity profiles in Fig. 7, obtained after 10 inertial periods with no pressure gradient forcing.

Ekman solution was derived. The upslope current is again steady, so (1) and (2) become

$$-\phi v = \Delta\rho g \sin\alpha + K\frac{\partial^2 u}{\partial z^2},$$

$$\frac{\partial v}{\partial t} + \phi u = K\frac{\partial^2 v}{\partial z^2}, \quad \text{and}$$

$$u\frac{\partial \Delta\rho}{\partial x} = K\frac{\partial^2 \Delta\rho}{\partial z^2},$$

where the density deficit of the current is also steady because there is a balance between diffusion and along-slope advection. This latter balance is achieved on short time scales compared with the inertial period, so the velocity profiles are of the same form as those depicted in Fig. 2c for the earliest stages of evolution, and the boundary layer is thinner than the Ekman layer. Thus, the Coriolis term is small in the upslope momentum budget, which reduces to a balance between buoyancy and friction. The density deficit and upslope momentum equations then form a coupled set that takes the same form as the earlier Ekman equations but with the across-slope velocity replaced by the density deficit:

$$-(g\sin\alpha)\Delta\rho = K\frac{\partial^2 u}{\partial z^2}, \quad \text{and}$$

$$\left(\frac{\partial \Delta\rho}{\partial x}\right)u = K\frac{\partial^2 \Delta\rho}{\partial z^2}.$$

The cross-slope momentum balance is now an uncoupled diffusion equation, as was previously the case for the density deficit and associated cross-slope geostrophic flow. The solution for the upslope current and density deficit takes the same form as the Ekman solution

$$u' = u_P \exp\left(\frac{-z}{d_P}\right)\sin\left(\frac{z}{d_P}\right), \quad \text{and}$$

$$\Delta\rho = \frac{\Delta\rho}{\Delta T_*}T_{*a}\exp\left(\frac{-z}{d_P}\right)\cos\left(\frac{z}{d_P}\right),$$

but with velocity and length scales now given by

$$u_P = \left(\frac{g\sin\alpha}{\partial\Delta\rho/\partial x}\right)^{1/2}\frac{\Delta\rho}{\Delta T_*}T_{*a}, \quad \text{and}$$

$$d_P = \left(\frac{4K^2}{g\sin\alpha\,\partial\Delta\rho/\partial x}\right)^{1/4}.$$

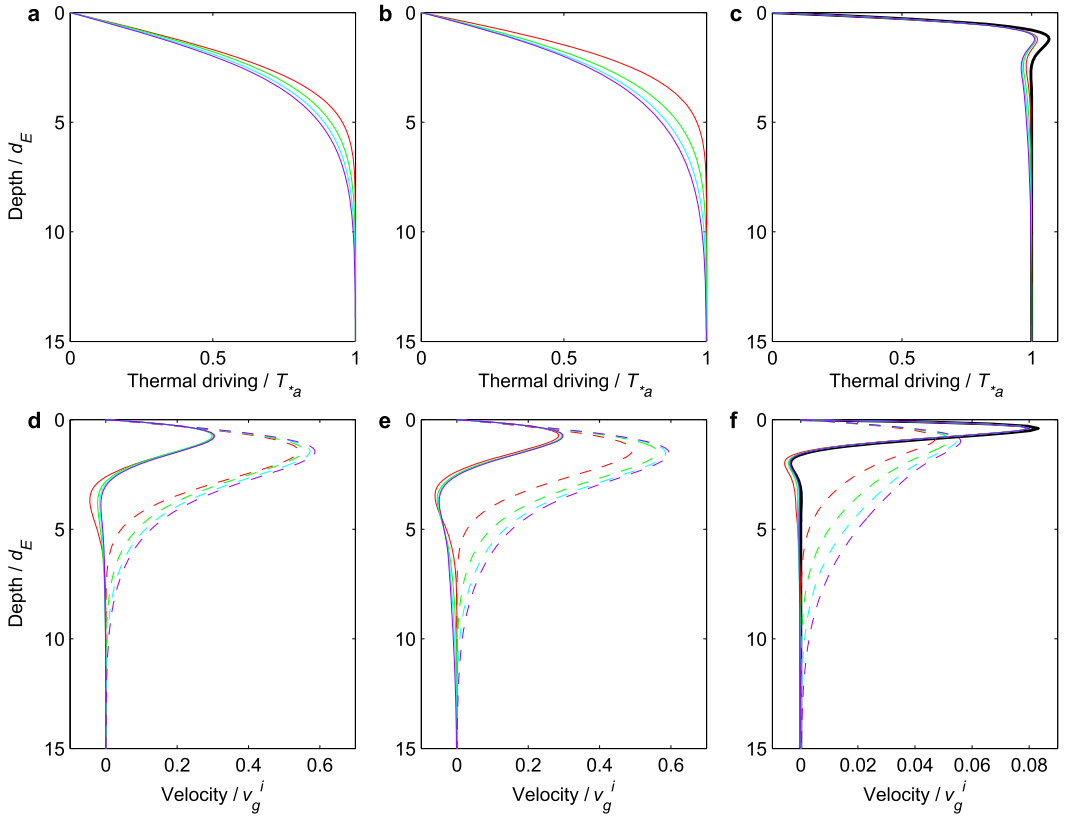

FIG. 9. (top) Thermal driving and (bottom) upslope (solid) and across-slope (dashed) velocity profiles for the case shown in Figs. 2a, 2d, 2c, and 2f when the diffusive growth of the boundary current is halted by (a),(d) vertical, (b),(e) across-slope, and (c),(f) along-slope heat advection. Different colors indicate the solution after 1, 2, 5, and 10 inertial periods. Thick black thermal driving and upslope velocity profiles in (c) and (f) show the steady Prandtl solution, discussed in the text. Note the differing horizontal scale in (f).

This analytical solution to the Prandtl model is plotted in Figs. 9c and 9f. The along-slope temperature gradient required to enter this regime can be estimated by comparing the length scales governing the Ekman and Prandtl solutions that must satisfy

$$d_P \leq d_E.$$

The inequality is satisfied when

$$\frac{\partial T_*}{\partial x} \geq \frac{\Delta T_*}{\Delta \rho} \frac{\phi^2}{g \sin\alpha}. \tag{9}$$

Figure 10 shows solutions for the region of parameter space either side of the equality. Analytical solutions for the steady Prandtl flow and temperature structure and for the steady upslope Ekman flow are shown. While the latter is the same in each case, the Prandtl length scale contracts as the temperature gradient increases and takes over as the limiting scale for the boundary layer. For low slopes typical of the underside of ice shelves, (9) yields unreasonably large temperature gradients of 10^{-2} to $10^{-3}\,^{\circ}\mathrm{C\,m^{-1}}$, suggesting that the solutions in Figs. 9c and 9f and 10c and 10f represent unlikely extremes. However, for quasi-vertical ice faces, the implied temperature gradient of $10^{-5}\,^{\circ}\mathrm{C\,m^{-1}}$ is readily attainable, suggesting that upslope advection is a candidate process for limiting the growth of the boundary current and confining it to the boundary layer in that case.

The inequality in (9) can also be written as

$$\left(g \frac{\partial \Delta\rho}{\partial z'}\right) \frac{\sin^2\alpha}{\phi^2} \geq 1, \tag{10}$$

which has the expected form of a Burger number for the boundary flow. For a nonuniform ambient water column there are two components to the gradient in the density deficit: one associated with density gradients within the boundary flow, and the other associated with density gradients within the ambient environment. If the latter

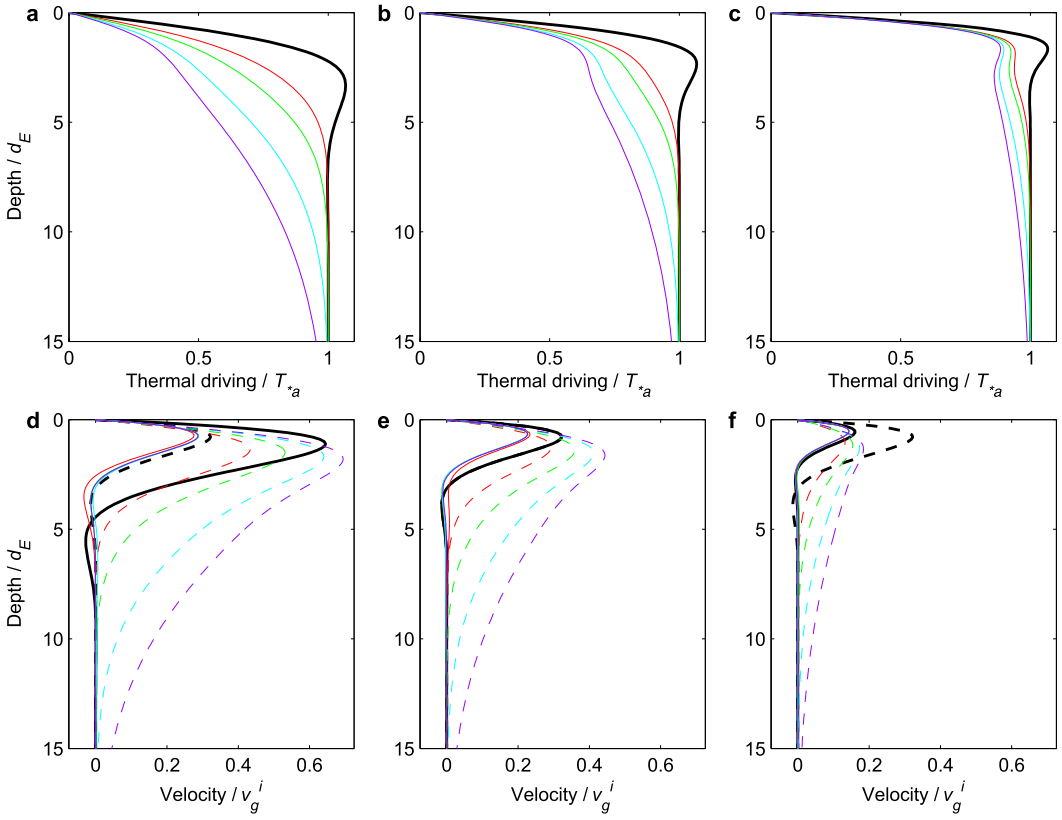

FIG. 10. (top) Thermal driving and (bottom) upslope (solid) and across-slope (dashed) velocity profiles for the case shown in Figs. 9c and 9f but with the along-slope density gradient chosen such that the ratio of Prandtl to Ekman length scales (d_P/d_E) is (a),(d) $\sqrt{2}$, (b),(e) 1, and (c),(f) $1/\sqrt{2}$. Different colors indicate the solution after 1, 2, 5, and 10 inertial periods. Thick black thermal driving and upslope velocity profiles show the steady, analytical Prandtl (solid) and Ekman (dashed) solutions, which overlie each other in (e) where the governing length scales are equal.

dominate, the term in parentheses on the left-hand side of (10) is the square of the buoyancy frequency associated with the ambient stratification. The buoyancy frequency is typically much greater than the inertial frequency, so with the restriction to uniform ambient fluid relaxed, the conclusion stands that while the Ekman solution is most appropriate for low slopes, for steep or vertical ice walls the Prandtl solution is more appropriate.

Figures 9 and 10 serve to emphasize some important points. Adding an advective term that can balance diffusive loss of heat to the ice shelf base is the only way to simulate a steady-state boundary current with the model presented here, without the lower boundary condition coming into play. Furthermore, advection acts to maintain stratification within the boundary current that would otherwise gradually diffuse away. By bringing additional heat to the boundary current, advection influences the melt rate at the ice–ocean interface. The melt rate is no longer simply a product of vertical diffusion, and no part of the boundary layer can be considered a constant flux layer (Figs. 11b,c). For the Prandtl solution in particular, the heat flux normal to the ice shelf base falls to a fraction of its value at the interface over a distance of a few meters (Fig. 11c). Similarly, the shear stress is a complex function of distance from the ice–ocean interface, with a minimum at the core of the upslope current (Figs. 11e,f). The absence of a constant flux layer and the minimum in the shear stress at the velocity maximum are often cited complications in the analysis of katabatic winds (Oerlemans 2010) that manifest themselves also in the problem of the ice shelf–ocean boundary current, particularly on a steep ice face.

5. Discussion

While the restriction to one-dimension represents a severe limitation of the model presented above, the results do yield some insight into aspects of ice shelf–ocean boundary flows that have received little attention previously. As with conventional buoyancy-driven slope

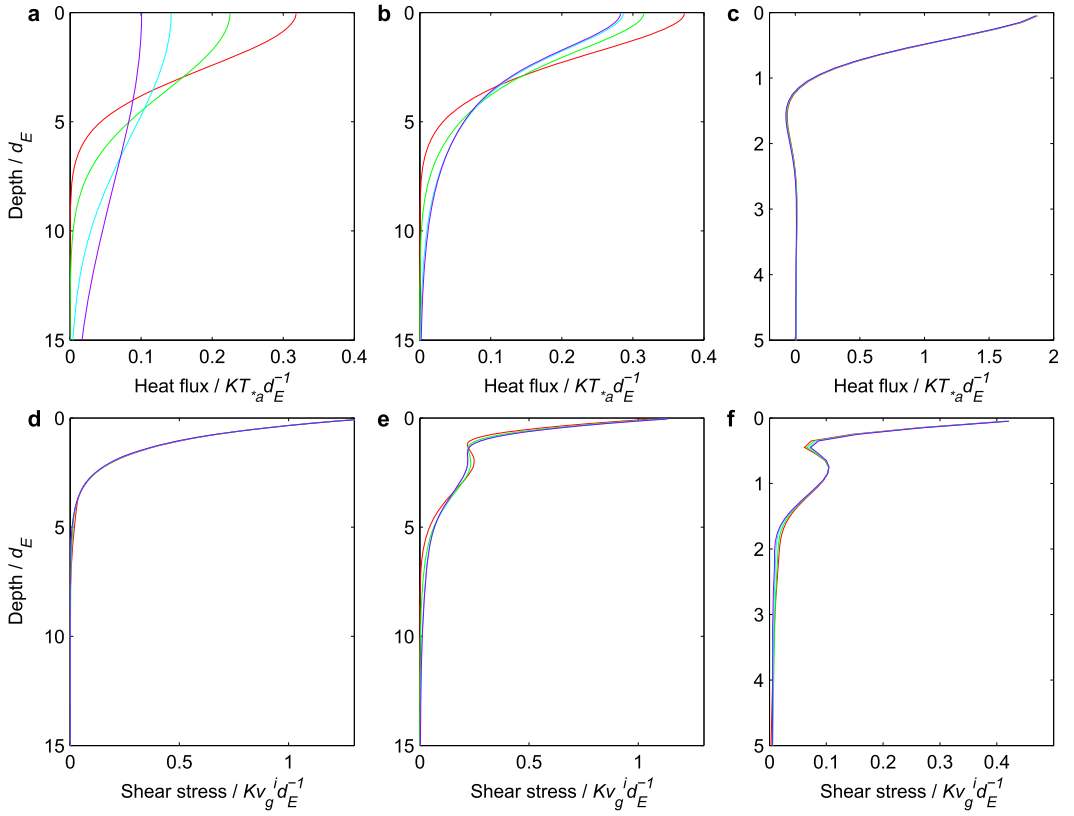

FIG. 11. Profiles of (top) vertical heat flux and (bottom) shear stress for the (a),(d) pressure gradient–forced solution shown in Figs. 2b and 2e and the sloping ice–ocean interface solutions in Figs. 9b, 9c, 9e, and 9f with (b), (e) cross-slope heat advection and (c),(f) upslope heat advection. Different colors indicate the solution after 1, 2, 5, and 10 inertial periods. Note the differing horizontal and vertical scales in (c) and (f).

currents, the flow can be decomposed into a geostrophic, across-slope boundary current and an embedded frictional boundary layer that carries the along-slope transport. The distinctive feature of the ice shelf–ocean boundary current is the stratification, which means that the geostrophic across-slope flow is itself a continuous function of depth across the boundary current. Despite this, the frictional deviations from geostrophy can be quantified through the application of classical Ekman theory, with scaling provided by the geostrophic velocity associated with the fixed density deficit at the ice–ocean interface. That result potentially allows the application of some fundamental results from ocean circulation theory to the sub–ice shelf environment. For example, from the Ekman solution follows a simple expression for the upslope transport within the boundary layer (Cushman-Roisin and Beckers 2011),

$$V_E = \frac{v_g^i d_E}{2},$$

that can be quantified in terms of the ambient ocean properties and the ice shelf basal slope:

$$V_E = g\frac{\Delta\rho}{\Delta T_*}\left(\frac{K}{2|f|^3}\right)^{1/2}\sin\alpha T_{*_a}.$$

For a laterally infinite ice shelf with no gradients in the y direction, this would be the only source of flow out of the cavity. The lowering of the surface elevation within the cavity caused by the outflow would generate a pressure gradient opposing the buoyancy-driven flow (as in Fig. 5d). Reduction of the upslope transport combined with a bottom Ekman transport into the cavity could then lead to a steady overturning circulation with opposing transports in the seabed and ice shelf boundary layers of magnitude $V_E/2$.

The slope of the ice shelf base introduces a background gradient in T_{*_a} associated with the fall in the freezing point temperature with increasing pressure. The result is a convergence in the upslope Ekman transport and pumping of water into the geostrophic flow. Similarly, changes in basal slope produce convergence or divergence in the Ekman flow, such that the curvature of the ice shelf base plays a role in driving Ekman pumping and suction analogous to that of the wind stress curl in

classical ocean circulation theory. The associated vertical velocity in the interior flow can be expressed as

$$w_E = -g\frac{\Delta\rho}{\Delta T_*}\left(\frac{K}{2|f|^3}\right)^{1/2}\frac{\partial}{\partial x}(\sin\alpha T_{*_a}).$$

If the background change in the freezing point temperature is the only contribution to changes in the ambient thermal driving and the ice shelf draft z_b' is expressed in terms of the original, unrotated coordinates, the vertical velocity becomes

$$w_E = -g\frac{\Delta\rho}{\Delta T_*}\left(\frac{K}{2|f|^3}\right)^{1/2}(T_{*_a}\nabla^2 z_b' - \rho_a g\lambda_3).$$

Typically ice shelves have steeper basal slopes where the ice is thicker, so the curvature is such that the gradient reduces in the upslope direction, driving Ekman pumping. For a steady circulation to develop requires a compensating pressure gradient–driven flow that acts to weaken the pumping from the ice–ocean boundary layer and generate a balancing Ekman suction into the seabed boundary layer.

Inverted channels carved into the base of ice shelves have received attention recently (Rignot and Steffen 2008; Dutrieux et al. 2013), but basic questions remain about how they influence the dynamics of the ice shelf–ocean boundary current. For topographic features that are wide compared with the internal Rossby radius of deformation, Wåhlin (2002) presented a theoretical treatment of geostrophic flow of dense water down channels cut into a continental slope. Wåhlin's (2002) steady along-channel flow is constructed by imposing cross-channel variations in boundary current thickness and hence pressure gradients that cancel the Ekman convergence driven by the curvature of the isobaths. For any channel geometry there is a maximum along-channel transport determined by the maximum gradient in boundary current thickness that can be contained within the channel. Similar principles should apply to flow within broad sub–ice shelf channels, with the added complication that the phase changes driven by the flow can modify the channel geometry.

A key simplification in the model is the assumption of constant viscosity/diffusivity. This is especially unrealistic close to the ice–ocean interface, so a quantitative discussion of the computed ice–ocean heat fluxes and associated melt rates is rather meaningless. The melt rates are directly proportional to the thermal driving gradient at the interface and so decay over time, unless a steady state is imposed by an arbitrary advection term. Nevertheless the computed current profiles give insight into the processes that drive turbulent mixing within the boundary flow. Current shear is stronger across the boundary layer than beyond it, while the stratification is relatively constant throughout the boundary current. That suggests that most turbulence closure models would produce higher viscosity/diffusivity within the boundary layer than deeper in the boundary current. A one-dimensional diffusion model would then yield a relatively well-mixed boundary layer and stronger stratification across the remainder of the boundary current, a structure that may not be dissimilar to the commonly assumed situation of a well-mixed layer underlain by a sharp pycnocline.

The foregoing comments notwithstanding, observations of the water column beneath ice shelves typically do not conform to the conventional view of a mixed layer, so the question remains as to what maintains stratification across the boundary layer. The answer to this, at least in the simplified framework of constant viscosity/diffusivity, is heat advection, either along or toward the ice shelf base. The earlier discussion of Ekman layer divergence suggested that the most common configuration of an ice shelf would drive advection away from the ice–ocean boundary, reducing the near-ice stratification. That leaves advection by the boundary current itself as the most likely candidate for maintaining the stratification. Plume models have already demonstrated the fundamental role of advection in controlling the along-flow temperature evolution and hence the large-scale patterns of melting and freezing. The model discussed in this paper suggests that it also plays a role in the transfer of heat across the ice–ocean boundary layer, complicating the problem of inferring heat fluxes from observations when the sampling is limited to individual vertical profiles.

6. Conclusions

As stated at the outset, the model discussed above is far from being a complete theory for the ice shelf–ocean boundary layer and current. In particular, it is not intended as a replacement for plume models but rather a complimentary analysis of the underlying equations. Current structure over the dimension that is depth averaged in plume models has previously been investigated in the context of well-mixed flows (Shapiro and Hill 1997; Wang et al. 2003; Cenedese et al. 2004), but the model presented here incorporates the effects of a stabilizing interfacial buoyancy flux. The simplification of constant viscosity/diffusivity means that little quantitative can be said about scalar profiles beneath an ice shelf but that simplification does allow an exploration of the most fundamental controls on the current structure. In this way the model starts to fill an important gap in our knowledge left by the complete absence of any observations of near–ice shelf current profiles.

A key result is the separation of the boundary current into an exterior geostrophic flow and an interior frictional boundary layer, features that are averaged together by depth integration in the plume equations. The upslope flow in the frictional boundary layer can be quantified through classical Ekman theory once the boundary current thickness exceeds the boundary layer thickness. Analogous results are obtained for conventional density currents on seabed slopes, but in the case of the ice shelf–ocean boundary current the Ekman transport remains steady, irrespective of subsequent evolution in the thickness of, and stratification across, the boundary current. The reason is that the Ekman response scales with the density deficit at the interface and that is fixed by the freezing point conditions that must prevail there. That simple result provides a potential link between low-order analyses of the ocean general circulation and the circulation within a sub–ice shelf cavity, with the interfacial conditions replacing wind stress curl as the driver of exchange between the boundary layer and the geostrophic flow beyond. A quantitative theory for the circulation in an idealized cavity, forced only by melting at the ice–ocean interface, would provide an invaluable test bed for numerical models.

The initial motivation for this study was an investigation of shear within the ice shelf–ocean boundary current that acts as the source of turbulent kinetic energy for mixing. The present model is only a starting point for this; a fuller investigation would require the addition of a turbulence closure scheme that relates viscosity/diffusivity to shear production and buoyancy suppression of turbulence. However, some general pointers emerge. A relatively well-mixed layer is likely to emerge from the one-dimensional diffusion problem, since the application of any turbulence closure model will yield higher viscosity/diffusivity within the frictional boundary layer than within the boundary current, where shear is generated only by the stratification. Along-slope advection is the strongest candidate for maintaining stratification within the boundary layer itself, so gradients in temperature and salinity across the boundary layer are likely to be stronger against steep or vertical ice faces.

The distinction in the mixing processes between the boundary layer and boundary current may help to explain one of the key failings of plume models. Most, if not all, theories result in one-way entrainment, so that once water is incorporated into the plume it continues to interact with the ice, even when the plume slows and thickens as it encounters the more gently sloping ice shelf base further from the grounding line. Mixing into the plume is determined by the shear instability at its outside edge; either the shear is sufficient to overcome the gravitational stability and drive entrainment or the interface is stable. Since diffusivity is implicitly assumed to be high within the plume, there is no mechanism to restratify the flow and detrain part of the plume. However, if vigorous mixing can only be sustained within the frictional boundary layer, convergence of the flow within that layer will lead to pumping of water into the geostrophic interior where it will cease to interact directly with the ice. It might be possible to capture these processes using a combination of both one-dimensional approaches to the ice shelf ocean interaction problem, using the plume concept to simulate the geostrophic boundary current but embedding within it a simple model or parameterization of the boundary layer.

Acknowledgments. I am grateful to Ed Bueler, University of Alaska Fairbanks, for MATLAB scripts that formed the basis for my numerical solution of the one-dimensional advection–diffusion problem. The constructive comments of two anonymous reviewers led to improvements in the clarity of the presentation.

REFERENCES

Cenedese, C., J. A. Whitehead, T. A. Ascarelli, and M. Ohiwa, 2004: A dense current flowing down a sloping bottom in a rotating fluid. *J. Phys. Oceanogr.*, **34**, 188–203, doi:10.1175/1520-0485(2004)034<0188:ADCFDA>2.0.CO;2.

Corr, H. F. J., A. Jenkins, K. W. Nicholls, and C. S. M. Doake, 2002: Precise measurement of changes in ice-shelf thickness by phase-sensitive radar to determine basal melt rates. *Geophys. Res. Lett.*, **29**, doi:10.1029/2001GL014618.

Cushman-Roisin, B., and J.-M. Beckers, 2011: *Introduction to Geophysical Fluid Dynamics*. 2nd ed. Academic Press, 828 pp.

Dansereau, V., P. Heimbach, and M. Losch, 2014: Simulation of subice shelf melt rates in a general circulation model: Velocity-dependent transfer and the role of friction. *J. Geophys. Res. Oceans*, **119**, 1765–1790, doi:10.1002/2013JC008846.

Depoorter, M. A., J. L. Bamber, J. A. Griggs, J. T. M. Lenaerts, S. R. M. Ligtenberg, M. R. van den Broeke, and G. Moholdt, 2013: Calving fluxes and basal melt rates of Antarctic ice shelves. *Nature*, **502**, 89–92, doi:10.1038/nature12567.

Dutrieux, P., D. G. Vaughan, H. F. J. Corr, A. Jenkins, P. R. Holland, I. Joughin, and A. H. Fleming, 2013: Pine Island Glacier ice shelf melt distributed at kilometre scales. *Cryosphere*, **7**, 1543–1555, doi:10.5194/tc-7-1543-2013.

Gade, H. G., 1979: Melting of ice in sea water: A primitive model with application to the Antarctic ice shelf and icebergs. *J. Phys. Oceanogr.*, **9**, 189–198, doi:10.1175/1520-0485(1979)009<0189:MOIISW>2.0.CO;2.

Garrett, C., P. MacCready, and P. Rhines, 1993: Boundary mixing and arrested Ekman layers: Rotating stratified flow near a sloping boundary. *Annu. Rev. Fluid Mech.*, **25**, 291–323, doi:10.1146/annurev.fl.25.010193.001451.

Hattermann, T., O. A. Nøst, J. M. Lilly, and L. H. Smedsrud, 2012: Two years of oceanic observations below the Fimbul Ice Shelf, Antarctica. *Geophys. Res. Lett.*, **39**, L12605, doi:10.1029/2012GL051012.

Holland, D. M., and A. Jenkins, 1999: Modeling thermodynamic ice–ocean interactions at the base of an ice shelf. *J. Phys. Oceanogr.*, **29**, 1787–1800, doi:10.1175/1520-0485(1999)029<1787:MTIOIA>2.0.CO;2.

Jenkins, A., 1991: A one-dimensional model of ice shelf-ocean interaction. *J. Geophys. Res.*, **96**, 20 671–20 677, doi:10.1029/91JC01842.

——, 2011: Convection-driven melting near the grounding lines of ice shelves and tidewater glaciers. *J. Phys. Oceanogr.*, **41**, 2279–2294, doi:10.1175/JPO-D-11-03.1.

——, H. F. J. Corr, K. W. Nicholls, C. L. Stewart, and C. S. M. Doake, 2006: Interactions between ice and ocean observed with phase-sensitive radar near an Antarctic ice shelf grounding line. *J. Glaciol.*, **52**, 325–346, doi:10.3189/172756506781828502.

MacAyeal, D. R., 1985: Evolution of tidally triggered meltwater plumes below ice shelves. *Oceanology of the Antarctic Continental Shelf*, S. S. Jacobs, Ed., Antarctic Research Series, Vol. 43, Amer. Geophys. Union, 133–143.

McPhee, M., 2008: *Air-Ice-Ocean Interaction: Turbulent Ocean Boundary Layer Exchange Processes*. Springer, 224 pp.

Nicholls, K. W., S. Østerhus, K. Makinson, T. Gammelsrød, and E. Fahrbach, 2009: Ice-ocean processes over the continental shelf of the southern Weddell Sea, Antarctica: A review. *Rev. Geophys.*, **47**, RG3003, doi:10.1029/2007RG000250.

Nof, D., 1983: The translation of isolated cold eddies on a sloping bottom. *Deep-Sea Res.*, **30**, 171–182, doi:10.1016/0198-0149(83)90067-5.

Oerlemans, J., 2010: *The Microclimate of Valley Glaciers*. Universiteitsbibliotheek Utrecht, 138 pp.

Price, J. F., and M. O. Baringer, 1994: Outflows and deep water production by marginal seas. *Prog. Oceanogr.*, **33**, 161–200, doi:10.1016/0079-6611(94)90027-2.

Pritchard, H. D., S. R. M. Ligtenberg, H. A. Fricker, D. G. Vaughan, M. R. van den Broeke, and L. Padman, 2012: Antarctic ice-sheet loss driven by basal melting of ice shelves. *Nature*, **484**, 502–505, doi:10.1038/nature10968.

Rignot, E., and K. Steffen, 2008: Channelized bottom melting and stability of floating ice shelves. *Geophys. Res. Lett.*, **35**, L02503, doi:10.1029/2007GL031765.

——, S. Jacobs, J. Mouginot, and B. Scheuchl, 2013: Ice-shelf melting around Antarctica. *Science*, **341**, 266–270, doi:10.1126/science.1235798.

Shapiro, G. I., and A. E. Hill, 1997: Dynamics of dense water cascades at the shelf edge. *J. Phys. Oceanogr.*, **27**, 2381–2394, doi:10.1175/1520-0485(1997)027<2381:DODWCA>2.0.CO;2.

Stanton, T. P., and Coauthors, 2013: Channelized ice melting in the ocean boundary layer beneath Pine Island Glacier, Antarctica. *Science*, **341**, 1236–1239, doi:10.1126/science.1239373.

van den Broeke, M. R., and N. P. M. van Lipzig, 2003: Factors controlling the near-surface wind field in Antarctica. *Mon. Wea. Rev.*, **131**, 733–743, doi:10.1175/1520-0493(2003)131<0733:FCTNSW>2.0.CO;2.

Wåhlin, A. K., 2002: Topographic steering of dense currents with application to submarine canyons. *Deep-Sea Res. I*, **49**, 305–320, doi:10.1016/S0967-0637(01)00058-9.

Wang, J., M. Ikeda, and F. J. Saucier, 2003: A theoretical, two-layer, reduced-gravity model for descending dense water flow on continental shelves/slopes. *J. Geophys. Res.*, **108**, 3161, doi:10.1029/2000JC000517.